Computational Materials Science 227 (2023) 112275

Contents lists available at ScienceDirect

Computational Materials Science

journal homepage: www.elsevier.com/locate/commatsci

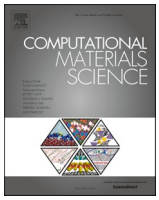

Full Length Article

Unveiling the multifaceted properties of a 3d covalent-organic framework: Pressure-induced phase transition, negative linear compressibility and auxeticity

Mustafa Erkartal

Department of Nanotechnology, Abdullah Gul University, Kayseri 38080, Turkey

ARTICLE INFO

Keywords:
Covalent-Organic Frameworks (COFs)
Phase transitions
High pressure
Negative linear compressibility
Auxeticity

ABSTRACT

High-pressure behavior and mechanical properties of a three-dimensional covalent-organic framework (NPN-1) were investigated by using different types of first principles molecular simulations. An irreversible pressure-induced first-order isosymmetric phase transition was predicted at 0.14 GPa. The subunit of NPN-1 retains its rigidity under pressure thanks to the strong covalent bonds. However, compression leads to significant tilting of the nitrophenyl groups. The mechanical properties of frameworks are highly anisotropic. Remarkably, both phases exhibit not only negative linear compressibility along the c-axis but also negative Poisson's ratio in certain directions. Detailed structural analysis revealed that the origin of the phase transition and anomalous mechanical properties of both phases are the wine-rack motif and strut-hinge mechanism. To the best of our knowledge, this study is the first report of such behavior in COFs, opening up new avenues for the exploration of COFs as materials for many promising applications.

1. Introduction

Open framework materials (OFMs), including both metal–organic frameworks (MOFs) and covalent organic frameworks (COFs), are a rapidly growing category of nanoporous materials. These materials are characterized by their supramolecular structures, which are composed of metal nodes and organic linkers that form a nanoporous crystalline structure. The nodes can be made up of transition metals (especially Zn, Zr, Co) or clusters in the case of MOFs, or main-group elements such as C, N, Si, and B in the case of COFs [1–3]. OFMs have attracted significant attention in recent years due to their unique properties such as high surface area, tunable pore size and shape, and adjustable chemical functionality. These properties make OFMs well suited for a variety of applications including gas storage [4,5] and separation [6,7], catalysis [8,9], and sensing [10,11].

Recently, researchers have been highly interested in studying the high-pressure behavior and mechanical properties of OFMs, as it can provide insight into the fundamental properties of these materials and their potential applications. When exposed to high pressure, OFMs can exhibit a variety of behaviors, including phase transitions that involve a change in crystal structure or formation of an amorphous phase [12–16], structural changes such as pore collapse or expansion [17–19], and abnormal mechanical properties such as the negative gas adsorption [20], auxeticity [21], or negative linear compressibility (NLC) [22–25]. Among them, negative linear compressibility (NLC), which is an unusual property in materials where the system expands in one direction when subjected to uniform compression, has the potential to be used in a wide range of applications in high-pressure environments, such as the development of advanced artificial muscles, highly accurate pressure sensors and durable shock-absorbing materials [26].

The structural flexibility of OFMs allows the framework angles to change rapidly with increasing pressure. This leads to a much larger NLC value than in traditional inorganic materials, but it also limits the range of pressures over which NLC behavior occurs [27]. Up to know, NLC phenomenon has been reported for several MOFs. The MIL-53 family is a well-known example of a material with a high degree of NLC, characterized by a compressibility of -28 TPa^{-1} in the pressure range of 0–3 GPa [28]. Another example is a framework similar to β-quartz, [InH(BDC)$_2$], which has been found to exhibit extremely high NLC of -62.4 TPa^{-1} due to a framework-hinging mechanism [29]. Zn-phosphanate, ZAG-4, also displays NLC of -18 TPa^{-1} at high pressure due to the structural transition involving reversible proton transfer [30]. Recent study have also shown that MFM-133 (Hf) exhibits NLC of -7.9 TPa^{-1} along the c-axis over the pressure range of 0–4.9 GPa, resulting from a wine-rack mechanism leading to distortion of the octahedral cage [23]. Additionally, MCF-34 has been found to exhibit a novel NLC behavior with a large value of -47.3 TPa^{-1}, which is attributed to the combination of orientations of four different types of wine-rack units [31]. Clearly, the wine-rack structural motif and the strut-hinges mechanism are the primary causes of negative linear compressibility in

https://doi.org/10.1016/j.commatsci.2023.112275
Received 24 February 2023; Received in revised form 11 May 2023; Accepted 17 May 2023
Available online 24 May 2023

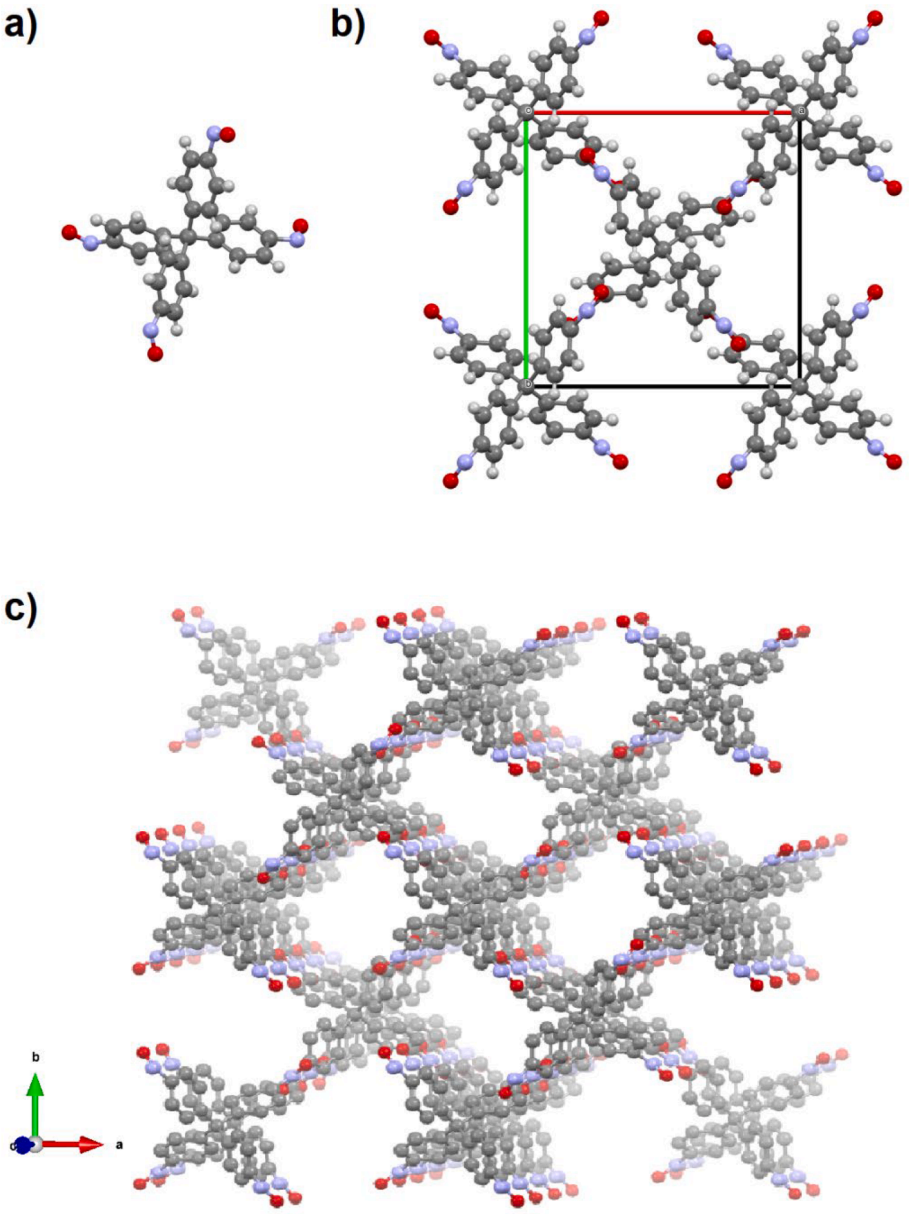

Fig. 1. (a) The monomer (Tetrakis(4-nitrosophenyl)methane) of NPN-1, (b) unit cell of NPN-1, (c) NPN-1 at ambient conditions viewed along the c axis, exhibiting the parallel channels. (C:grey; N:blue; O:red; H:white). (For interpretation of the references to color in this figure legend, the reader is referred to the web version of this article.)

metal–organic frameworks (MOFs).

Despite this significant interest in the mechanical properties and pressure-dependent characteristics of various porous MOF structures, the knowledge of the mechanical properties of COFs is limited to a small number of theoretical predictions [32–34] and only one experimental study [35] that have been conducted. Very recently, it has been reported both experimentally and computationally that 3D COF-320 exhibits atropisomerism and gas adsorption-induced structural phase transition [36]. The main issue that hinders the study of mechanical properties of COFs is the difficulty in synthesizing them as single crystals, as COF syntheses often produce polycrystalline or amorphous materials [37]. This makes it impossible to use experimental methods, such as DAC, to determine the pressure-dependent mechanical properties of COFs. Additionally, structures modeled from PXRD data have limitations, such as uncertain atomic positions, geometric parameters, and guest arrangements within the pores, as well as complexities from interpenetrated frameworks and disorder. These limitations make it challenging to conduct computational studies due to the lack of a consistent initial structure.

In this study, the behavior of a 3-dimensional COF with wine rack topology, NPN-1, whose mechanical properties have not yet been experimentally proven, under high pressure were investigated by quantum calculations. In this context, the elastic constants of both structures were first calculated using initial geometries derived from single crystals. In order to investigate how COFs change structurally when exposed to isotropic pressure, the ground-state structures are subjected to full structural relaxations under the isotropic compression. Finally, AIMD simulations were performed in an isobaric-isothermal (NPT) ensemble at 300 K and varying isotropic pressures to demonstrate that our findings are independent of the simulation method and parameters we used, as well as to explore the effect of temperature on the behavior of the material.

2. Methodology

All first principles calculations were performed using a plane wave based density functional theory (DFT) as implemented in Quantum Espresso (QE) package [38]. The electron–ion interactions were described by projector augmented wave (PAW) potential [39]. The exchange–correlation potential was treated within the generalized gradient approximation (GGA) with Perdew-Burke-Ernzerhof (PBE) parametrization [40]. The dispersive interactions were incorporated within the GGA using a semi-empirical potential (DFT-D2) as defined by Grimme [41]. The Broyden-Fletcher-Goldfarb-Shanno (BFGS) minimization scheme is used for the full structural optimization [42]. Convergence criteria for residual forces and energy difference between two consecutive optimization steps were set to 10^{-3} eV/Å and 10^{-6} eV, respectively. A Monkhorst-Pack [43] k-space mesh of 2 × 2 × 4 in reciprocal space was used for the Brilloun zone integration. The kinetic energy and charge density cut-off were 80 and 600 Rydberg, respectively. By using these parameters, first of all, the experimentally derived unit cell of NPN-1 was fully relaxed by optimizing both atomic positions and unit cell parameters. Secondly, the pressure dependence of elastic constants of NPN-1 was investigated. To determine elastic constants, the lattice is strained and internal degrees of freedom of the crystal structure were allowed to relax in the elastic regime. Then, elastic constants were calculated through the changes in stress tensor with respect to applied strain. These calculations were performed by using the thermo_pw package, and details of method can be found in [44]. Thirdly, the hydrostatic pressure was applied on the framework. To this end, a series of successive enthalpy minimization calculation for each value of pressure were performed by starting from the optimized structure. Thus, the evolution of unit parameters as a function of pressure was obtained. Finally, to both validate our zero-Kelvin calculations and mimic an isotropic diamond-anvil experiment, the first principles molecular dynamics (FPMD) simulations of NPN-1 were performed with SIESTA package [45], which is the LCAO (Linear Combination of Atomic orbitals)-based DFT code. The Perdew-Burke-Ernzerhof (PBE) generalized gradient approximation (GGA) [40], the norm-conserving Troulier-Martins pseudopotentials [46], and the double-ζ polarized orbitals for all atoms (C,N,O,H) were preferred in the simulations. Real space integration was carried out on an ordered grid corresponding to a plane wave cut off of 350 Ry; a very large plane-wave expansion is crucial to guarantee convergence in the calculated total energy and atomic forces. An empirical correction for the dispersive interactions by D2 scheme of Grimme was also used for FPMD simulations. Isobaric–isothermal (variable-cell NPT) was carried out by using a single unit cell of NPN-1. The dynamics were performed using a time step of 1 fs, in which a Nosé thermostat controls the temperature and a Parrinello-Rahman barostat [47] controls hydrostatic compression. The identical Parinello-Rahman mass and Nose mass of 150 Ry × fs^2 were found as optimum coupling constants. While temperature was set at 300 K, the several of hydrostatic pressure (0 GPa, 0.3 GPa, 0.5 GPa and 1 GPa) was applied on the framework. At each pressure step, a period of 12,000 MD steps (namely 12 ps) was performed to obtain equilibrium state. The Mercury program for visualization, the PLATON code [48] for the symmetry analysis of high pressure phases, the ELATE code [49] for derivation of mechanical properties and the ATOMSK [50] for post-processing QE obtained data were used.

3. Results and discussion

NPN-1 (nitroso polymer network) is the first three-dimensional COF whose structure can be fully characterized using single-crystal X-ray diffraction (SXRD) [37]. The framework with transazodioxide linkages are prepared through crystallization from a solution of tetra-functional nitroso, resulting in a diamondoid network. The diamondoid network of NPN-1 has an open structure that allows for four-fold interpenetration along the c-axis (Fig. 1). NPN-1 is packed in the tetragonal crystal system with $P\bar{4}b2$ space group [51].

Table 1
Lattice parameters of NPN-1.

Parameter	a = b (Å)	c (Å)	α = β = γ (°)	Volume (Å^3)	Density (g cm^{-3})	SAV (%)	S. Group
NPN1-exp	13.15	7.98	90	1381.18	1.05	36.3	P −4b 2
NPN-1/ PAW-PBE-D2	13.38	7.76	90	1391.89	1.04	36.4	P −4b 2
NPN-1-hd/ PAW-PBE-D2	11.44	7.92	90	1036.60	1.40	NA	P −4b 2

In order to relax NPN-1, experimentally reported structure was subjected a variable-cell optimization, i.e. optimizing both atomic positions and unit cell parameters. The calculated lattice parameters are in well agreement with the experimental crystallographic values (Table 1), and resulting optimized structure has the same space group with starting geometry (namely $P\bar{4}b2$) according to the symmetry analysis. Then the optimized structure was exposed to full structural relaxation under hydrostatic compression in the range of 0 to 5 GPa. This mimics the application of pressure at low temperatures and has been found to match experimental results for many frameworks materials in previous studies [52–54]. The evolution of the unit cell volume and lattice parameters as a function of isotropic compression are shown in Fig. 2 and listed in Table S2. Obviously, the compression causes a drastic decrease in volume of approximately 27% at 0.2 GPa, signifying a pressure-induced phase transition (Fig. 2a). The initial and final phases have the same space group symmetry, indicative of an isosymmetric phase transition (IPT). This type of phase transition, termed as type 0, does not involve the changes in the space group or occupied Wyckoff sites. IPT is in contrast to other types of phase transitions, such as type I, II, or III, which involve diffusionless transformations.[55] It is commonly observed in amorphous systems and electronic transitions, but few cases have been reported where the transformation is primarily structural [56,57].

After the phase transition, that is, beyond 0.2 GPa, the structure becomes less compressible. Up to 5 GPa, the unit cell volume only decreases by 9%. According to the symmetry analysis, no amorphization or structural failure is observed in this compression region, and the structure maintains its initial symmetry. No significant change in the unit cell volume is observed upon decompression, indicating that the phase transition is irreversible. The symmetry analysis reveals that the structure has tetragonal $P\bar{4}b2$ space group symmetry. However, this structure, which has a higher density than NPN-1 at ambient conditions as a result of compressed volume, will be referred to as NPN-1-hd (hd denotes high density) in the rest of the article. The calculations were repeated using different functional (BLYP) and pseudopotential (Vandebilt-ultrasoft) to assess the reliability of the results due to the lack of experimental data. The findings obtained with BLYP-USP correlated exactly with those of PBE-PAW, except for a slight overestimation of the lattice parameters, demonstrating the validity of the results (Table S1 and Fig. S1).

To elucidate the origin of the phase transition, the behavior of cell parameters under compression was investigated. As seen in Fig. 2a, the unit cell shrinks by about 15% along a- and b-axes and expands by 2% along the c-axis, indicating that NPN-1 shows NLC. Since NPN-1 has the wine-rack motif (Fig. 3a), NLC accompanied IPT can be explained by the strut-hinge mechanism. According to the strut-hinge model, NLC is initiated when the increase in hinge angle surpass the deformation of strut [58]. To determine if the model can account for our observations, we plotted the strut (r_{ab}), the distance between the nearest tetrahedral node, and the hinge (θ), the angle between the two struts, as a function

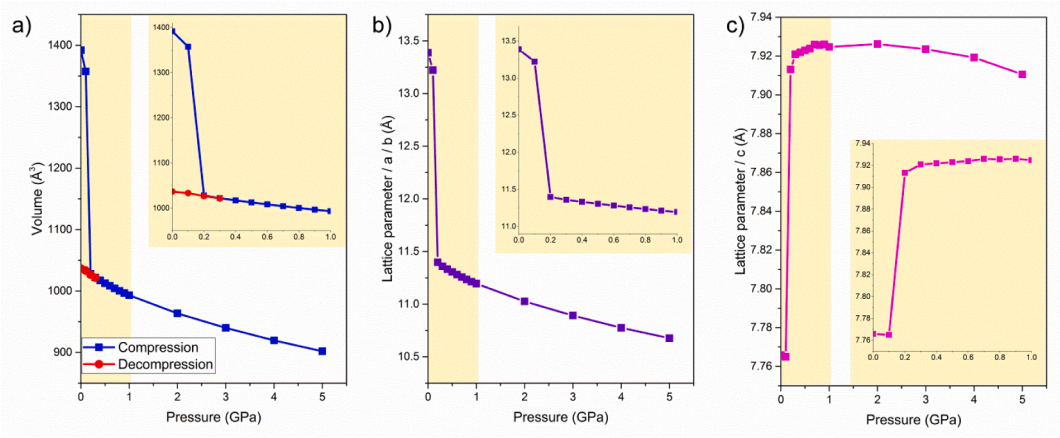

Fig. 2. The evolution of the (a) unit cell volume and (b, c) lattice parameters under isotropic compression.

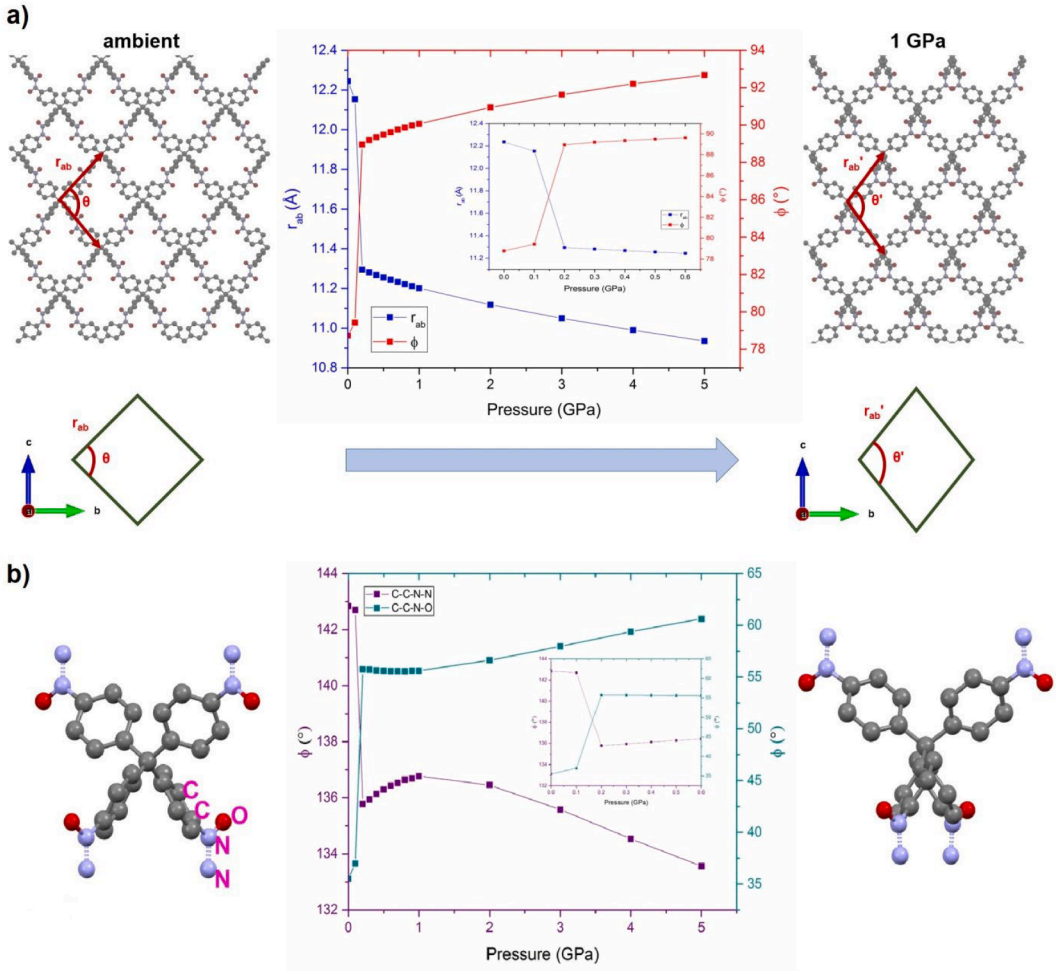

Fig. 3. (a) Wine-rack motif of NPN-1 along a-axis, and dependence of strut length and hinge angle on pressure. (b) The evolution of the nitroso monomer and dihedral angles under pressure.

of pressure (Fig. 3a). The evolution of both parameters under compression is similar to the pressure-dependent pattern of unit cell parameters. Up to 0.2 GPa, where the phase transition occurs, the hinge angle rapidly increases by 13%, while the strut length is shortened by % 7, confirming that the strut-hinge mechanism is the origin of the NLC-accompanied first-order phase transition. After the phase transition, the lattice parameters maintain their trend even though their variation decreases. However, a shrinking is also observed along the c-axis beyond 3 GPa.

Pressure can cause the bond lengths to change in the structure, resulting in the breaking of existing bonds or the formation of new bonds, as well as the tilting of the structures depending on the degree of freedom. Therefore, bond lengths, bond angles and dihedral angles were also investigated depending on the pressure to further examine the effects of compression on the structure. No significant elongation or shortening of the N=N and C–N bonds was observed before and after the

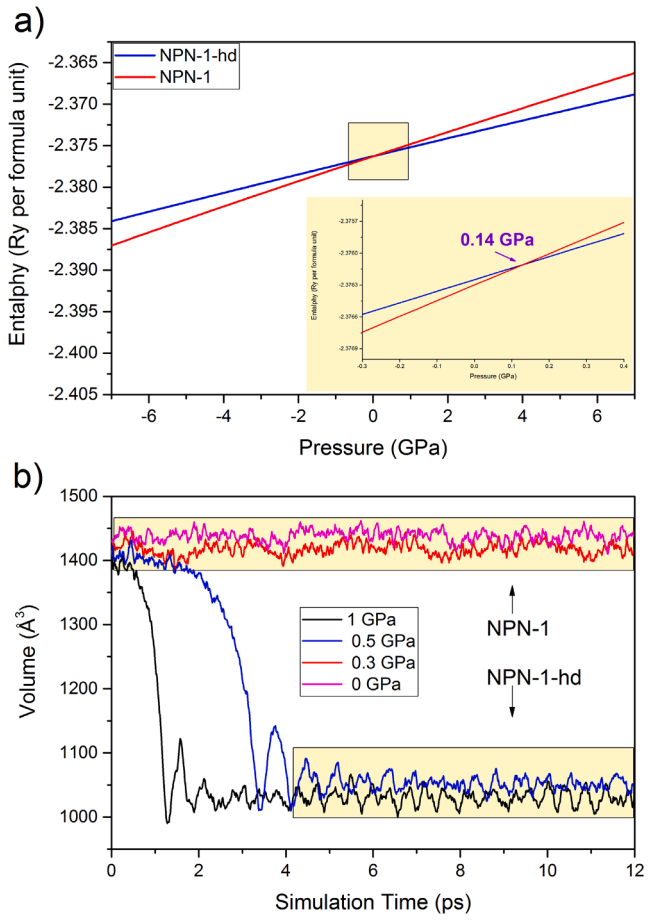

Fig. 4. (a) The calculated enthalpies NPN-1 and NPN-1-hd as a function of pressure. The curves cross at 0.14 GPa. (b) The evolution of the of unit cell volume of NPN-1 during FPMD at 300 K and different pressures.

phase transition. Likewise, the bond angles remain almost the same in the studied pressure region and the monomer maintains its almost-perfect tetrahedral geometry. Clearly, NPN-1 and NPN-1-hd have the same short-range order (see Fig. S5 and TableS S3–S5). According to these results, it can be concluded that the sub-unit of NPN-1 maintains its rigidity under pressure due to the strong covalent bonds. However, compression caused significantly tilting of the nitrophenyl groups. The quantity of this tilting is characterized by the pressure dependent changes of the C–C–N–N and C–C–N–O dihedral angles (Fig. 3b). Due to the rotational ability of the C–N bond, 70% tilting is observed to tolerate the compression, which is also the source of the strut-hinge mechanism.

Two thermodynamic theorems can be used to accurately determine the phase transition pressure of NPN-1 to NPN-1-hd: (i) at a given pressure and at zero temperature, the phase with the lowest enthalpy is the most stable, (ii) the critical pressure can be easily determined by comparing the enthalpy values of the two phases at the structural transition point, since the crystals have the same enthalpy value at this point. The Gibbs free energy (G = H-TS) is equivalent to enthalpy at absolute zero (H = E + PV, where E, V, and P represent energy, volume, and external pressure, respectively). Thus, various constants volume calculations were performed, and then the energy-volume data was

Table 3
Mechanical Properties of NPN-1 and NPN-1-hd.

Elastic Property		NPN-1	NPN-1-hd
Young Modulus, E(GPa)	E_{max}	27.08	29.76
	E_{min}	1.08	8.90
Shear Modulus G(GPa)	G_{max}	12.46	17.47
	G_{min}	0.29	2.77
Linear Compressibility, β (TPa^{-1})	B_{max}	32.12	17.05
	β_{min}	−20.05	−1.81
Poisson's ratio, ν	ν_{max}	2.40	1.16
	ν_{min}	−1.38	−0.33

fitted to the Murnaghan equation of state equation. The enthalpies of two NPN-1 phases as a function of pressure were illustrated in Fig. 4a. Clearly, the enthalpy crossover at 0.14 GPa denotes the critical pressure of IPT of NPN-1 to NPN-1-hd. As expected, NPN-1 is stable below the critical pressure; NPN-1-hd is stable above it. FPMD simulations were performed at 300 K under isotropic pressure both to take into account the thermal effects in the phase transition and to test the reliability of our method due to the lack of available experimental data. FPMD confirmed a first-order isosymmetric phase transition from NPN-1 to NPN-1-hd beyond 0.3 GPa (Fig. 4b). On the other hand, the over-estimation of the critical pressure can be attributed to the relatively short simulation time, which refers to a very rapid rate of pressurization or decompression, which does not allow sufficient time for physical relaxation or rearrangements to occur, and can lead to frozen states in simulations.

Elastic stiffness constants are important indicators of a solid's mechanical properties, including stability, stiffness, and directional dependence of elastic modulus. Therefore, the elastic constants of both NPN-1 and NPN-1-hd were determined using the non-volume conserving method. Since both phases have the tetragonal symmetry they have six independent elastic constants, i.e., C_{11}, C_{33}, C_{44}, C_{66}, C_{12}, C_{13}, and C_{16} (Table 2). To be mechanically stable, the calculated zero-pressure single-crystal elastic constants C_{ij} of a tetragonal (I) crystal must satisfy the following the Born-Huang stability criteria [59]:

$$C_{11} > |C_{12}|,$$
$$2C_{13}^2 < C_{33}(C_{11} + C_{12}),$$
$$C_{44} > 0,\ C_{66} > 0$$

The Born-Huang criteria states that a crystal is mechanically stable if its Gibbs free energy is at a minimum compared to any other state caused by infinitesimal strain [59]. For our case, both NPN-1 and NPN-1-hd meet these criteria, therefore, they are considered mechanically stable.

The presence of NLC has been linked to other unusual mechanical behaviors, such as high levels of mechanical anisotropy, unusual Poisson's ratio values, negative thermal expansion, and a tendency towards dynamic instability [26]. Hence, the tensorial analysis was used to determine the directional Young's modulus, shear modulus, linear compressibility, and Poisson's ratio of both phases from the elastic stiffness matrices. The extreme values of these parameters are summarized in Table 3. The highest values for the Young' moduli (E_{max}) for the both phases are the result of compression along the direction of the interpenetration of the monomers, [1 1 2]. However, the minimum values of it (E_{min}) for both phases are along the hinge direction, ⟨1 0 0⟩.

Table 2
Single-crystal elastic stiffness coefficients (C_{ij}) of NPN-1 and NPN-1-hd.

	C_{11}	C_{33}	C_{44}	C_{66}	C_{12}	C_{13}	C_{16}
NPN-1	25.18424	45.94124	12.45684	5.94124	24.612	29.903	0
NPN-1-hd	33.7867	52.14248	17.4734	3.7954	28.24627	32.07894	0

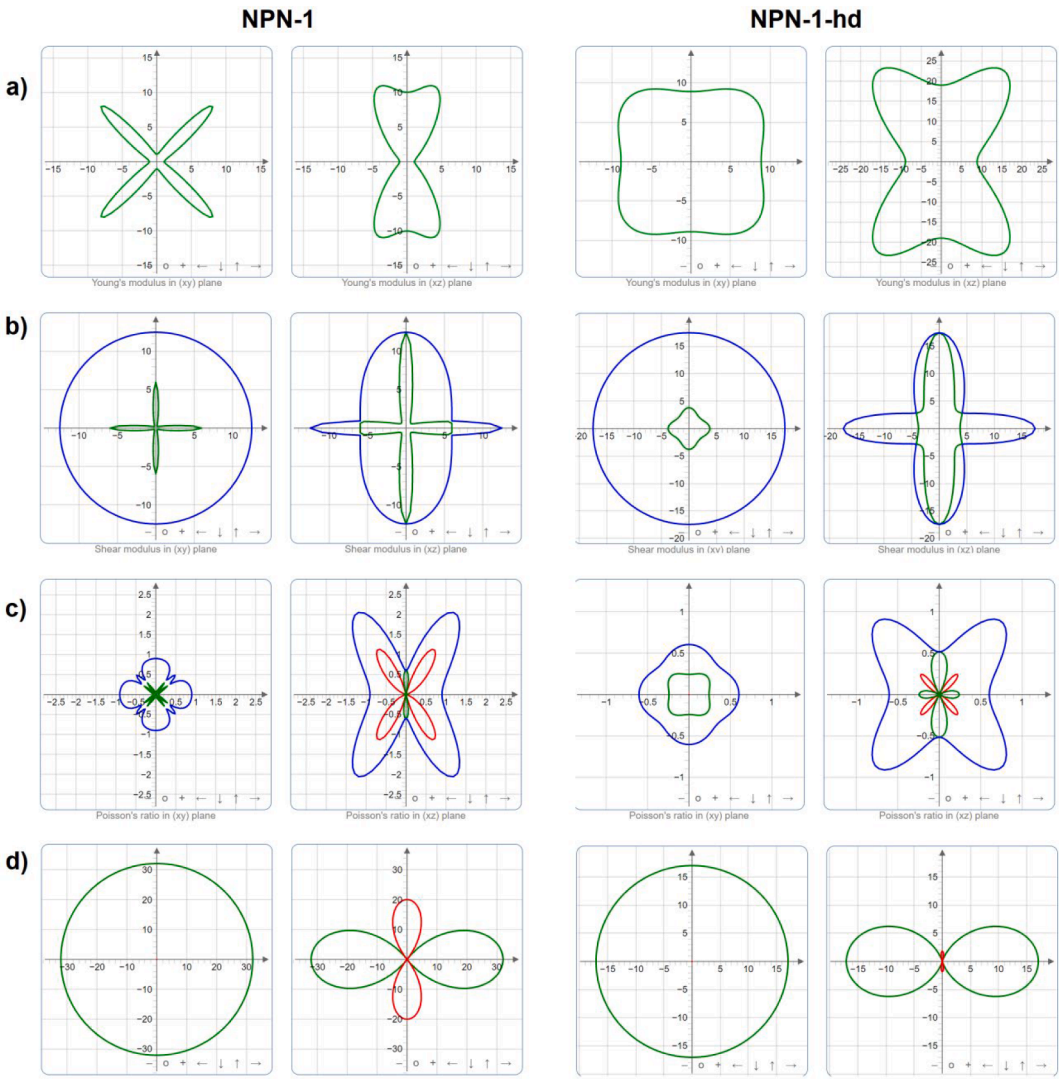

Fig. 5. Two dimensional maps of (a) Young' moduli, (b) Shear moduli, (c) Poisson' ratios and linear compressibilities for NPN-1 and NPN-1-hd. In (b) the blue outer line and the green inner line denotes the maximum and minimum values, respectively. In spherical coordinates, finding ν involves an additional dimension beyond the θ (ranging from 0 to π) and φ (ranging from 0 to 2π) coordinates, which can be described by the angle χ (ranging from 0 to 2π). The blue color in (c) represents the surface obtained at the highest value of χ, while the green (red) lobes indicate the positive (negative) values of ν at the lowest value of χ.In (c) the green line shows the positive LC whereas the red line shows the negative LC. (For interpretation of the references to color in this figure legend, the reader is referred to the web version of this article.)

Although the maximum values of E are similar for each phases with NPN-1-hd being slightly higher owing to higher density, NPN-1 has quite low minimum Young' modulus (Emin = 1.08 GPa) due to the relatively higher flexibility and porosity (Fig. 5a). The maximum shear modulus in both NPN-1 and NPN-1-hd is found along the c-axis, with NPN-1-hd having a higher value. However, the structures have the lowest shear modulus in the plane where the parallel channels are located. Notably, NPN-1 has a remarkably low shear modulus with a minimum value of 0.29 GPa (Fig. 5b). Such a low shear modulus is similar to that previously reported for ZIF-3 with tetragonal symmetry [21]. The less stability of NPN-1 to shear strain can be attributed to strut-hinge mechanism and porosity. Indeed, the loss of porosity after the phase transition in NPN-1, as shown in the SAV results, supports this argument.

Materials with a negative Poisson's ratio, known as auxetic materials, have garnered significant attention from researchers due to their exceptional benefits in sensing technology [60]. The positive Poisson's ratio is defined as the ratio of transverse contraction to longitudinal extension in a material when stretched. Thus, auxetic materials are expected to expand in the transverse direction when stretched in the longitudinal direction, which is the opposite of what is seen in most materials. However, auxetic materials are less common compared to non-auxetic materials [60,61]. Remarkably, NPN-1 and NPN-1-hd exhibits exceptional Poisson's ratios, with NPN-1 having extremely high negative values ($\nu_{max} = -1.38$) (Fig. 5c). This is also attributed to wine-rack motif and strut-hinge mechanism in the framework. Finally, the compressibility of both phases was calculated. With the values we obtained, it was confirmed that both structures shows positive linear compressibility in the $\langle 1\,0\,0 \rangle$ direction, and negative linear compressibility in the $\langle 0\,0\,1 \rangle$ direction. When a structural phase transition occurs in conjunction with NLC behavior, a similar underlying mechanism can cause NLC to be observed at both low and high pressures. However, hardening and less compressibility of MOF-like porous structures after phase transition may lead to the disappearance or decrease of NLC [22,27]. Similarly, NPN-1 has a very high NLC (-20.85 TPa^{-1}) along the c-axis, while NPN-1-hd shows a very modest NLC (-1.81 TPa^{-1}) behavior (Fig. 5d).

4. Conclusion

In conclusion, this study presents an in-depth investigation of the high-pressure behavior of a 3D COF, named as NPN-1, by using first principles calculations. The results show that the NPN-1 undergoes an irreversible first-order isosymmetric phase transition in conjunction with negative linear compressibility, a property rarely observed in conventional materials. NPN-1-hd, the higher density analogue of NPN-1 formed as a result of this phase transition, has the same bond lengths as NPN-1 and the same tetrahedral geometry in the short-range order. In additional to NLC, these two structures exhibit a negative Poisson's ratio, another anomalous mechanical property, as evidenced by the results of elastic tensor analyses. The wine rack motif and strut-hinge mechanism of the structure were found to be the driving forces behind both the phase transition and the anomalous mechanical properties. In the absence of experimental data, multiple calculation methods were utilized to confirm the validity of the results, including first-principles molecular dynamics simulations. To the best of our knowledge, this is one of the first reports of such properties in a COF, opening up new avenues for exploring the relationship between structure and mechanical behavior in this class of materials. Further experimental studies are needed to validate the computational results, but this work provides a valuable foundation for future work in this area.

CRediT authorship contribution statement

Mustafa Erkartal: Conceptualization, Investigation, Methodology, Resources, Software, Visualization, Writing – review & editing.

Declaration of Competing Interest

The authors declare that they have no known competing financial interests or personal relationships that could have appeared to influence the work reported in this paper.

Data availability

The data that support the findings of this study are available on request from the corresponding author.

Acknowledgements

The calculations were run on The Scientific and Technological Research Council of Turkey (TÜBİTAK) ULAKBILIM, High Performance and Grid Computing Center (TRUBA) and AGU-HPC resources.

Appendix A. Supplementary material

See supplementary material for the detailed description of the structural features for NPN-1 and NPN-1-hd. Supplementary data to this article can be found online at https://doi.org/10.1016/j.commatsci.2023.112275.

References

[1] M.D. Allendorf, R.H. Dong, X.L. Feng, S. Kaskel, D. Matoga, V. Stavila, Chem. Rev. 120 (2020) 8581–8640.
[2] K.Y. Geng, T. He, R.Y. Liu, S. Dalapati, K.T. Tan, Z.P. Li, S.S. Tao, Y.F. Gong, Q. H. Jiang, D.L. Jiang, Chem. Rev. 120 (2020) 8814–8933.
[3] H. Furukawa, K.E. Cordova, M. O'Keeffe, O.M. Yaghi, Science 341 (2013) 974.
[4] H. Li, K.C. Wang, Y.J. Sun, C.T. Lollar, J.L. Li, H.C. Zhou, Mater. Today 21 (2018) 108–121.
[5] H. Furukawa, O.M. Yaghi, J. Am. Chem. Soc. 131 (2009) 8875–8883.
[6] R.B. Lin, S.C. Xiang, W. Zhou, B.L. Chen, Chem 6 (2020) 337–363.
[7] M. Tabatabaii, M. Khajeh, A.R. Oveisi, M. Erkartal, U. Sen, ACS Omega 5 (2020) 12202–12209.
[8] Y.S. Wei, M. Zhang, R.Q. Zou, Q. Xu, Chem. Rev. 120 (2020) 12089–12174.
[9] Z.S. Chen, J.Y. Wang, M.J. Hao, Y.H. Xie, X.L. Liu, H. Yang, G.I.N. Waterhouse, X. K. Wang, S.Q. Ma, Nat. Commun. 14 (2023) 1106.
[10] H.Y. Li, S.N. Zhao, S.Q. Zang, J. Li, Chem. Soc. Rev. 49 (2020) 6364–6401.
[11] L.L. Guo, L. Yang, M.Y. Li, L.J. Kuang, Y.H. Song, L. Wang, Coord. Chem. Rev. 440 (2021), 213957.
[12] M. Erkartal, M. Durandurdu, Mater. Chem. Phys. 240 (2020), 122222.
[13] M. Erkartal, M. Durandurdu, ChemistrySelect 3 (2018) 8056–8063.
[14] F. Colmenero, V. Timon, Appl. Sci.-Basel 12 (2022) 10413.
[15] Z.H. Shi, K.Y. Weng, N. Li, Molecules 28 (2023) 22.
[16] S.A. Moggach, T.D. Bennett, A.K. Cheetham, Angew. Chem.-Int. Ed. 48 (2009) 7087–7089.
[17] G. Ferey, C. Serre, Chem. Soc. Rev. 38 (2009) 1380–1399.
[18] Z. Su, Y.R. Miao, G.H. Zhang, J.T. Miller, K.S. Suslick, Chem. Sci. 8 (2017) 8004–8011.
[19] A.U. Ortiz, A. Boutin, F.X. Coudert, Chem. Commun. 50 (2014) 5867–5870.
[20] S. Krause, V. Bon, I. Senkovska, U. Stoeck, D. Wallacher, D.M. Tobbens, S. Zander, R.S. Pillai, G. Maurin, F.X. Coudert, S. Kaskel, Nature 532 (2016) 348–352.
[21] M.R. Ryder, J.C. Tan, Dalton Trans. 45 (2016) 4154–4161.
[22] D.Q. Jiang, T. Wen, Y.Z. Guo, J. Liang, Z.M. Jiang, C. Li, K. Liu, W.G. Yang, Y. G. Wang, Chem. Mater. 34 (2022) 2764–2770.
[23] Y. Yan, A.E. O'Connor, G. Kanthasamy, G. Atkinson, D.R. Allan, A.J. Blake, M. Schroder, J. Am. Chem. Soc. 140 (2018) 3952–3958.
[24] W. Li, M.R. Probert, M. Kosa, T.D. Bennett, A. Thirumurugan, R.P. Burwood, M. Parinello, J.A.K. Howard, A.K. Cheetham, J. Am. Chem. Soc. 134 (2012) (1943) 11940–11941.
[25] M. Erkartal, Mater. Today Commun. 35 (2023), 106054.
[26] A.B. Cairns, A.L. Goodwin, PCCP 17 (2015) 20449–20465.
[27] I.E. Collings, A.L. Goodwin, J. Appl. Phys. 126 (2019), 181101.
[28] P. Serra-Crespo, A. Dikhtiarenko, E. Stavitski, J. Juan-Alcaniz, F. Kapteijn, F. X. Coudert, J. Gascon, CrstEngComm 17 (2015) 276–280.
[29] Q.X. Zeng, K. Wang, B. Zou, J. Am. Chem. Soc. 139 (2017) 15648–15651.
[30] A.U. Ortiz, A. Boutin, K.J. Gagnon, A. Clearfield, F.X. Coudert, J. Am. Chem. Soc. 136 (2014) 11540–11545.
[31] Q.X. Zeng, K. Wang, B. Zou, Acs Mater Lett 2 (2020) 291–295.
[32] H.Y. Li, J.L. Bredas, Chem. Mater. 33 (2021) 4529–4540.
[33] J. Zhang, PCCP 20 (2018) 29462–29471.
[34] W. Zhou, H. Wu, T. Yildirim, Chem. Phys. Lett. 499 (2010) 103–107.
[35] J.H. Sun, A. Iakunkov, I.A. Baburin, B. Joseph, V. Palermo, A.V. Talyzin, Angew. Chem.-Int. Ed. 59 (2020) 1087–1092.
[36] C. Kang, Z. Zhang, S. Kusaka, K. Negita, A.K. Usadi, D.C. Calabro, L.S. Baugh, Y. Wang, X. Zou, Z. Huang, R. Matsuda, D. Zhao, Nat. Mater. 22 (2023) 636–643.
[37] X.Y. Guan, F.Q. Chen, Q.R. Fang, S.L. Qiu, Chem. Soc. Rev. 49 (2020) 1357–1384.
[38] P. Giannozzi, S. Baroni, N. Bonini, M. Calandra, R. Car, C. Cavazzoni, D. Ceresoli, G.L. Chiarotti, M. Cococcioni, I. Dabo, A. Dal Corso, S. de Gironcoli, S. Fabris, G. Fratesi, R. Gebauer, U. Gerstmann, C. Gougoussis, A. Kokalj, M. Lazzeri, L. Martin-Samos, N. Marzari, F. Mauri, R. Mazzarello, S. Paolini, A. Pasquarello, L. Paulatto, C. Sbraccia, S. Scandolo, G. Sclauzero, A.P. Seitsonen, A. Smogunov, P. Umari, R.M. Wentzcovitch, J. Phys.-Condens. Mat. 21 (2009), 395502.
[39] P.E. Blochl, Phys. Rev. B 50 (1994) 17953–17979.
[40] J.P. Perdew, K. Burke, M. Ernzerhof, Phys. Rev. Lett. 77 (1996) 3865–3868.
[41] S. Grimme, J. Comput. Chem. 27 (2006) 1787–1799.
[42] S.R. Billeter, A.J. Turner, W. Thiel, PCCP 2 (2000) 2177–2186.
[43] H.J. Monkhorst, J.D. Pack, Phys. Rev. B 13 (1976) 5188–5192.
[44] A. Dal Corso, J. Phys.-Condens. Mat. 28 (2016), 075401.
[45] P. Ordejon, E. Artacho, J.M. Soler, Phys. Rev. B 53 (1996) 10441–10444.
[46] N. Troullier, J.L. Martins, Phys Rev B 43 (1991) 1993–2006.
[47] M. Parrinello, A. Rahman, J. Appl. Phys. 52 (1981) 7182–7190.
[48] A.L. Spek, J. Appl. Crystallogr. 36 (2003) 7–13.
[49] R. Gaillac, P. Pullumbi, F.X. Coudert, J. Phys.-Condens. Mat 28 (2016), 275201.
[50] P. Hirel, Comput. Phys. Commun. 197 (2015) 212–219.
[51] D. Beaudoin, T. Maris, J.D. Wuest, Nat. Chem. 5 (2013) 830–834.
[52] J. Maul, M.R. Ryder, M.T. Ruggiero, A. Erba, Phys. Rev. B 99 (2019), 014102.
[53] P.S. Ghosh, I. Ponomareva, J. Phys. Chem. Lett. 12 (2021) 7560–7565.
[54] P.S. Ghosh, I. Ponomareva, J. Phys. Chem. Lett. 13 (2022) 3143–3149.
[55] A.G. Christy, Acta Crystall. Sect. B-Struct. Sci. 51 (1995) 753–757.
[56] Y.Q. Tang, C. Lopez-Cartes, M.A. Aviles, J.M. Cordoba, CrstEngComm 20 (2018) 5562–5569.
[57] S.M. Clarke, B.A. Steele, M.P. Kroonblawd, D.Z. Zhang, I.F.W. Kuo, E. Stavrou, J. Phys. Chem. B 124 (2020) 1–10.
[58] R. Caruana-Gauci, E.P. Degabriele, D. Attard, J.N. Grima, J. Mater. Sci. 53 (2018) 5079–5091.
[59] F. Mouhat, F.X. Coudert, Phys. Rev. B 90 (2014), 224104.
[60] G.N. Greaves, A.L. Greer, R.S. Lakes, T. Rouxel, Nat. Mater. 10 (2011) 823–837.
[61] R.H. Baughman, S.O. Dantas, S. Stafstrom, A.A. Zakhidov, T.B. Mitchell, D.H. E. Dubin, Science 288 (2000) 2018.